Computational characterization of plasma effects in ultrafast laser irradiation of spherical gold nanostructures for photothermal therapy

Computational characterization of plasma effects in ultrafast laser irradiation of spherical gold nanostructures for photothermal therapy

Ali Hatef[1], Behafarid Darvish[1], Adam Burke[1], Adrien Dagallier[2] and Michel Meunier[2]

[1] Nipissing Computational Physics Laboratory (NCPL), Department of Computer Science and Mathematics, Nipissing University, North Bay, Ontario, P1B 8L7, Canada
[2] Laser Processing and Plasmonics Laboratory (LP2L), Engineering Physics Department, École Polytechnique de Montréal, Montréal, Québec, H3C 3A7, Canada

E-mail: alih@nipissingu.ca

CrossMark

Abstract
Ultrashort pulsed lasers can provide high peak intensity with low pulse fluence. This makes them an ideal choice in photothermal therapy and applications where damage to the surrounding material needs to be minimized. Depending on the peak intensity, the ultrashort pulsed laser's interaction with matter can lead to plasma formation through nonlinear effects such as multiphoton and impact electron excitation. The capability of the spherical gold nanoparticles, as the most employed nanoparticle so far for photothermal therapy, to enhance and strongly localize the incident laser field leads to plasma formation around the particles at even lower pulse fluences. Under certain circumstances, during the pulse duration, this plasma can absorb more energy than the nanoparticle itself. Consequently, the absorbed energy by the generated plasma can act as an energy source for different phenomena such as the evolution of the temperature distribution, thermoelastic stress generation, and stress-induced bubble formation. In this paper, we study the plasma-mediated interaction of a 45 fs pulsed laser with two types of spherical gold nanoparticles in water: solid nanoparticle and core–shell (silica–gold) nanoparticle. We use a numerical framework based on the finite element method (FEM) to compare energy deposition profiles in these nanoparticles and in their surrounding plasma, by focusing on the impact of the nanoparticle size and the laser fluence. Our calculations show that the maximum energy deposition in plasma occurs in core–shell nanoparticles with a diameter of 130 nm and the ratio of core to shell radius of 0.8 and in solid nanoparticles with a diameter of 170 nm.

Keywords: spherical gold nanoparticle, solid and core–shell nanoparticle, energy deposition, plasmon resonance, plasma dynamics, ultrashort pulsed laser, photothermal therapy

(Some figures may appear in colour only in the online journal)

Introduction

Ultrashort pulsed lasers that can provide a high peak intensity with a low pulse fluence have been widely used in photothermal therapy [1], primarily because the ultrashort laser's

pulse duration is shorter than the heat diffusion time of the interacting materials. This results in diminished thermal shock and reduced collateral damage to the laser-irradiated materials, including biological tissues [2]. This interaction may also involve plasma formation, which occurs due to the

J. Phys. D: Appl. Phys. **49** (2016) 105401

A Hatef *et al*

'breakage' of molecular and atomic bonds mostly within the focal region of the water-based medium. This occurs when the local field intensity reaches its threshold value and generates a highly localized free electron density within the focal region. The origin of this plasma formation is the excitation of the electrons into the conduction band of the water considered as an amorphous semiconductor with a 6.5 eV gap [1]. This electron excitation occurs through various physical processes, including multiphoton ionization, quantum tunnelling, and impact ionization [3]. Once generated, the plasma keeps absorbing energy until the end of the pulse, leading to a highly localized energy deposition in the focal volume.

Recently, gold nanoparticles (NPs) have shown novel properties that provide highly localized, functional, and multifunctional platforms because of the collective oscillation of their conduction electrons triggered by the incident electromagnetic field [4]. This collective oscillation, known as localized surface plasmon resonance, can convert the incident light to photothermal energy within the gold NPs. This energy deposition can be widely used in biomedical applications, particularly in photothermal therapy, tissue welding and optoporation of cells for drug delivery [5–7]. In addition, gold NPs can generate strongly enhanced electromagnetic fields in close vicinity of their surface. In this process, called near field enhancement (FE), the ratio of the scattered field amplitude to the incident field amplitude increases several times in the vicinity of the gold NPs [8].

Taking advantage of the FE, the ultrashort pulsed laser interaction with the gold NPs ensures a highly localized plasma in the close vicinity of the particles with low laser fluence while minimizing potential damage on living tissues [7]. Therefore, by choosing an appropriate gold NP and incident laser fluence, we can achieve more energy deposition in the plasma surrounding gold NP rather than in the gold NP itself.

Among all gold NPs, solid nanoparticles (SNPs) and core–shell nanoparticles (CSNPs) exhibit a unique combination of small size, spherical shape and a strong, tunable absorption band in the near infrared (NIR) tissue optical window ($\lambda = 700$–900 nm). Even at low laser intensities, these features give a large penetration depth that ranges from a few millimetres to several centimetres, depending on the tissue type [9, 10].

In an experimental framework, one can explore the plasma generation in the vicinity of gold NPs by studying the induced plasma-mediated nanobubbles in the region [3, 11]. For instance, through experiments, it has been proven that by irradiating SNPs (diameter = 100 nm) with a linearly polarized pulsed laser fluence ranging from 100 to 200 mJ cm^{-2}, nanobubbles of ~0.5 to 1.5 μm in diameter are detected. This corresponds to energy deposition within the SNPs and the surrounding plasma ranging from 0.5 pJ to 1.2 pJ and 2 pJ to 22 pJ, respectively [3]. The maximum bubble radius is proportional to the total energy deposition in both SNPs and the surrounding plasma. As a result, using an equivalent total energy range should produce similar sizes of nanobubbles. These nanobubbles can be used in nanomedicine applications such as cell optoporation and transfection [7, 12].

In this paper, we use a theoretical model for a linearly polarized 45 femtosecond (fs) pulsed laser's interaction with the gold NPs (SNPs and CSNPs) surrounded by water, in the tissue therapeutic optical window ($\lambda = 800$ nm). Here, the main emphasis is on the impact of gold NP's geometrical parameter and the laser's fluence on the photothermal energy deposition in the plasma as well as in the NPs. For each particle a specific range of laser fluence is considered to ensure the production of sufficient electron density in the vicinity of gold NPs in such a way that the energy deposition in the plasma becomes comparable to or even higher than that in the gold NPs.

Theoretical approach

In the following equations, further information for the different parameters and variables is available in table 1.

Photonics

Electromagnetic interaction between the laser pulse and the nanostructure-water system is calculated using equation (1), called the Helmholtz equation [13]:

$$\nabla \times (\mu_r^{-1} \nabla \times \vec{E}) - k_0^2 \varepsilon_r \vec{E} = 0 \,, \tag{1}$$

where μ_r is the relative permeability of the materials and it is taken as unity, $\vec{E}$ is the electric field distribution, k_0 is the wavenumber, σ is the conductivity, ω is the angular frequency and ε_r is the complex frequency-dependent relative permittivity. ε_r is assumed to be constant in gold during the irradiation. For water, ε_r is derived from the Drude permittivity shown in equation (2) [14]:

$$\varepsilon_r = \varepsilon_\infty - \frac{n_e e^2}{\epsilon_0 m(\omega^2 + j\omega\gamma_c)}, \tag{2}$$

where ε_∞ stands for the water permittivity, n_e is the plasma density, e is the electron charge, ϵ_0 is the vacuum permittivity, m is the electron mass and γ_c is the electron collision frequency.

The Helmholtz equation is solved in a spherical domain, ten times larger than the gold NP, with an outer perfectly matched layer domain and a scattering boundary condition to emulate an infinite computation domain. This equation gives the electromagnetic field, hence the field enhancement, everywhere in the computational domain [15]. This study focuses on the early stages of the bubble formation; therefore a study domain bigger than the expected bubble size (a few micrometres in diameter [16]) is not necessary.

The scattering and absorption cross-sections are defined as $\sigma_{scat} = \frac{Q_{scat}}{I_0}$ and $\sigma_{abs} = \frac{Q_{abs}}{I_0}$, where the energy scattered and absorbed by the gold NPs are calculated as follows [17]:

$$Q_{scat} = \frac{1}{2} Re \left[\iint \vec{E}_{scat} \times \vec{H}_{scat} \cdot \vec{n} \, ds \right] \tag{3}$$

Table 1. Input parameters and functions.

Electromagnetism

Parameter	Symbol	Value
Gold relative permittivity	$\varepsilon_{r,\text{Au}}(\lambda)$	Interpolated from [19]
Gold electrical conductivity	$\sigma_{\text{Au}}(\lambda)$	(Interpolated from [19]) S m^{-1}
Gold relative permeability	$\mu_{r,\text{Au}}$	1
Water thermal conductivity	$k_{\text{w}}(T)$	$(-8.691 \times 10^{-1} + (8.949 \times 10^{-3})T - (1.584 \times 10^{-5})T^2 + (7.975 \times 10^{-9})T^3)\,\text{W m}^{-1}\text{K}^{-1}$
Water relative permittivity	$\varepsilon_{r,\text{w}}$	1.764
Water electrical conductivity	σ_{w}	0 S m^{-1}
Water relative permeability	$\mu_{r,\text{w}}$	1
Silica relative permittivity	$\varepsilon_{r,\text{s}}$	1.5
Silica electrical conductivity	σ_{s}	0
Silica relative permeability	$\mu_{r,\text{s}}$	1

Thermodynamics

Parameter	Symbol	Value
Gold heat capacity	$C_{p,\text{Au}}(T)$	$((399\,352)T^{-2} + 114.9 + (3.229 \times 10^{-2})T)\,\text{J kg}^{-1}\,\text{K}^{-1}$
Gold density	$\rho_{\text{Au}}(T)$	$(19501 - (6.934 \times 10^{-1})\,T - (2.042 \times 10^{-4})\,T^2 + (4.298 \times 10^{-8})T^3)\,\text{kg m}^{-3}$
Gold thermal conductivity	$k_{\text{Au}}(T)$	$(330.6 - (2.537 \times 10^{-2})\,T - (8.191 \times 10^{-5})\,T^2 + (6.793 \times 10^{-8})\,T^3 - (2.154 \times 10^{-11})\,T^4)\,\text{W m}^{-1}\text{K}^{-1}$
Water heat capacity	$C_{p,\text{w}}(T)$	$(12\,010 - (80.41)T + (3.099 \times 10^{-1})T^2 - (5.382 \times 10^{-4})\,T^3 + (3.625 \times 10^{-7})\,T^4)\,\text{J kg}^{-1}\text{K}^{-1}$
Water density	$\rho_{\text{w}}(T)$	$(838.5 + (1.401)\,T - (3.011 \times 10^{-3})\,T^2 + (3.718 \times 10^{-7})\,T^3)\,\text{kg m}^{-3}$
Silica heat capacity	C_{s}	703 J kg^{-1} K^{-1}
Silica density	ρ_{s}	2100 kg m^{-3}

Plasma dynamics

Parameter	Symbol	Value
Collision cross-section [20]	σ_a	2×10^{-19} m^2
Free electron mass	m_{e}	9.109×10^{-31} kg
Collision ionization cross-section [21]	σ_0	8.87×10^{-22} m^2
Electron velocity [22]	v_{e}	Calculated from the density of state g(ε)
Ionization potential [1]	Δ	6.5 eV
Plasmon frequency [23]	ω_{p}	$\sqrt{\dfrac{n_{\text{e}}e^2}{m_{\text{e}}\varepsilon_0}}$
Degree of ionization [24]	Z	1
Valence electron density [1]	n_0	6.68×10^{22} cm^{-3}
Neutral atom density	n_{a}	$(n_0 - n_{\text{e}})/2$
Plasma recombination time [1]	τ_{e}^{ω}	2×10^{-9} cm^3 s^{-1}
Normalized kinetic energy [25]	β	$u/\widetilde{\Delta}$
Collision ionization frequency [25]	ν_{ci}	$n_a\sigma_0 v_{\text{e}}((7.5\beta - 1)\sqrt{\beta\pi}\,e^{-1/\beta}(3.5\beta^2 - 3\beta - 1)erfc(1/\sqrt{\beta}))$
Recombination rate [1]	S_{rec}	$\tau_{\text{e}}^{\omega}n_{\text{e}}^2$
Electromagnetic rate of work [13]	S_{EM}	$\dfrac{1}{2}Re(J*\!\cdot\!E)$
Collision ionization rate [25]	S_{coll}	$\nu_{\text{ci}}n_{\text{e}}$

(*Continued*)

Table 1. *(Continued)*

Plasma dynamics		
Parameter	Symbol	Value
Plasma collision frequency with ionized species [24]	ν_{ei}	$\min\left(\dfrac{\omega_p}{\sqrt{6}}, \dfrac{Ze^4 n_e \Lambda}{3\varepsilon_0{}^2 \sqrt{m_e}(2\pi T_e)^{3/2}} \right)$
Coulomb logarithm [24]	Λ	$\dfrac{1}{2}\ln\left(1 + \left(\dfrac{b_{\max}}{b_{\min}} \right)^2 \right)$
Maximal impact factor [24]	$b_{\max}$	$\left(\dfrac{n_e e^2}{\varepsilon_0 k_{\text{B}} \sqrt{T_e{}^2 + T_{\text{F}}{}^2}} + \dfrac{n_e e^2}{\varepsilon_0 k_{\text{B}} T_m} \right)^{-\frac{1}{2}}$
Minimal impact factor [24]	$b_{\min}$	$\max\left(\dfrac{Ze^2}{4\pi\varepsilon_0 m_e v_e{}^2}, \dfrac{h}{2m_e v_e} \right)$
Fermi temperature	T_{F}	$\dfrac{\hbar^2}{2m_e k_{\text{B}}}(3\pi^2 n_e)^{2/3}$
Plasma collision frequency with neutral species [25]	ν_{en}	$n_a \sigma_a v_e$
Electron–ion energetic coupling [26]	Q_{ei}	$3\dfrac{m_e}{m_i} n_e(\nu_{\text{ei}} + \nu_{\text{en}})k_{\text{B}}(T_e - T_m)$
Energetic loss by plasma radiation [26]	Q_{rad}	$\dfrac{1}{4\pi\varepsilon_0} \dfrac{4e^2(k_{\text{B}}T_e)^2}{\sqrt{3}\,\hbar m_e c^3} n_e(\nu_{\text{ei}} + \nu_{\text{en}})$
Electron current density [22]	j^n	$D_e \nabla n_e$
Electron density diffusion (Maxwell distribution)	D_e	$\dfrac{k_{\text{B}}T_e}{m_e(\nu_{\text{ei}} + \nu_{\text{en}})}$
Thermal current density [22]	j^q	$D_u \nabla u$
Electron energy density diffusion (Maxwell distribution)	D_u	$\dfrac{5}{3}D_e$

$$Q_{\text{abs}} = \frac{1}{2}Re\left[\iint \vec{E}_{\text{tot}} \times \vec{H}_{\text{tot}} \cdot \vec{n}\,\mathrm{d}s \right]. \tag{4}$$

These formulas assume the medium is dissipative, where $\vec{E}$ and $\vec{H}$ are respectively the electric and magnetic field, scattered or total, and $\vec{n}$ is a unit vector normal to the particle surface. I_0 is taken as $\frac{1}{2}\epsilon_0 n_{\text{water}} E_0^2$, where n_{water} is the refractive index of water. The total extinction cross-section is $\sigma_{\text{ext}} = \sigma_{\text{scat}} + \sigma_{\text{abs}}$.

Thermal evolution

The femtosecond laser pulse intensity is written as follows:

$$I(t) = \frac{F_L}{\sqrt{2\pi}t_\sigma} \exp\left(\frac{-(t - t_0)^2}{2t_\sigma^2} \right), \tag{5}$$

with $t_\sigma = {}^{t_1}/_{2\sqrt{2}\ln(2)}$, where t_1 is the laser pulse width defined as the full width at half maximum of the Gaussian temporal profile, t_0 is the time position of the centre of the peak and F_L is the fluence of the incident laser. The pulse width in this paper is in the femtosecond range, which is much shorter than the phonon thermalization time (~1–3 ps). To study the evolution of the gold NP temperature, we use a Two-Temperature Model (TTM) in which a temperature for the gold electrons and one for the gold lattice is calculated as seen in equations (6) and (7) [18]:

$$C_e(T_e)\frac{\partial T_e}{\partial t} = \nabla \cdot (k_e \cdot \Delta T_e) - G \cdot [T_e - T_l] + S(t) \tag{6}$$

$$C_l(T_l)\frac{\partial T_l}{\partial t} = \nabla \cdot (k_l \cdot \Delta T_l) + G \cdot [T_e - T_l]. \tag{7}$$

C_i, k_i and T_i, where $i = $ e (electron) or l (lattice), are respectively the heat capacity, thermal conductivity and temperature which is time- and space-dependent. G is the electron–phonon coupling coefficient. The term $G \cdot [T_e - T_l]$ accounts for the energy exchange between the electrons and the lattice. $S(t)$ is the absorbed laser energy.

Plasma dynamics

Two coupled diffusion equations are used to describe the plasma evolution in water: one for the plasma's electronic density (equation (8)), and the other one for the plasma's kinetic energy (equation (9)) [3],

$$\frac{\partial n_e}{\partial t} + \nabla \cdot j^n = S_{\text{photo}} + S_{\text{coll}} - S_{\text{rec}} \tag{8}$$

$$\frac{\partial u}{\partial t} + \nabla \cdot j^q = \frac{1}{2}\text{Re}(J * \cdot E) - Q_{\text{ei}} - Q_{\text{rad}} - \widetilde{\Delta}S_{\text{coll}}. \tag{9}$$

In these equations, u is the plasma kinetic energy, S_{photo} is the full Keldysh ionization term [3], S_{coll} is the collision ionization term accounting for the excitation of new electrons by colliding with highly energetic electrons and $\tilde{\Delta}$ is the extraction potential. S_{rec} is the recombination term and Q_{ei} is the electron–ion energetic coupling while Q_{rad} is the radiative loss. j^n is the electron current density and j^q is the thermal current density.

The power density deposited in the system is evaluated with the following formulas [3]:

- For water:

$$Q_{total\ plasma} = Q_{plasma} + Q_{photo} \tag{10}$$

$$Q_{plasma} = \frac{1}{2}\sigma_{plasma}|E|^2 \tag{11}$$

$$Q_{photo} = S_{photo}\frac{n_0 - n_e}{n_0}\Delta. \tag{12}$$

- For the nanoparticle:

$$Q_{AuNP} = \frac{1}{2}\sigma_{Au}|E|^2, \tag{13}$$

Q_{plasma} is the power density absorbed by the plasma through inverse bremsstrahlung process, and Q_{photo} is the power density that is required for the photoionization of the water molecules.

These expressions are then integrated over their whole computation domain to yield the total power deposition. The energy is then given by integration from 0 fs to ten times the pulse duration. All details are summarized in table 1.

Results and discussions

Field enhancement, absorption, scattering and extinction

In this study, the SNPs are solid spherical nanoparticles that vary in size from 50 nm to 250 nm in diameter; while, the CSNPs, contain a core and a shell of SiO$_2$ (silica) and Au (gold) respectively and vary in size from 50 nm to 200 nm in diameter, with aspect ratio (AR) = 0.8 (the ratio of core to shell radius). CSNPs consisting of a gold shell and a dielectric core have been extensively studied in optical and biomedical applications because their surface plasmon resonance can be very well tuned to the biological transparency window [27]. SiO$_2$ has become a common core material for gold CSNPs, since being first synthesized in 1998 [28]. In this paper, there is a difference between the refractive index of the core of CSNP (SiO$_2$) and its surrounding medium (water). This leads to an increase in the FE factor in the vicinity of CSNPs. If the core's refractive index was similar to that of the medium (water in our case), the maximum FE factor would be around 7.8 while with the core being SiO$_2$, this value changes to ~8.1; since the energy deposition in plasma is nonlinearly and directly dependent on the FE factor, this increase in FE factor, due to the SiO$_2$ core, enhances the

energy deposition in plasma. Please note that the gold shell thicknesses are ranging from 5 nm to 20 nm for the considered gold CSNPs with an AR of 0.8 and diameters ranging from 50 nm to 200 nm, respectively. From [29] we see that the quantum effect in silver particles becomes important for diameters below 5 nm. By developing a framework that includes quantum contributions, this reference also manages to explain the experimental measurements in [30]. Therefore, we chose to neglect the quantum contribution and apply the classical theory to the gold NPs in this study.

Here, both gold NPs are characterized by an experimental local dielectric function obtained from nanometre-sized samples [19]. The surrounding medium for both gold NPs is water, which makes the obtained results more practical for biological applications [31]. These nanostructures are irradiated with a linearly polarized plane wave at wavelength $\lambda = 800$ nm. The laser has a Gaussian form with ultrashort pulse width of 45 fs. In table 1, we have provided all the parameters used in our simulations.

The gold NPs' geometric parameters such as the AR and diameter have a significant impact on the electric FE near the surface of the gold NPs, which is a key component to plasma formation. The effect of the gold NP's size on the electric FE is shown in figures 1(a) and (b), where we show the maximum electric FE factor (E/E_0) versus the diameter for both CSNP with AR = 0.8, and SNP. Here, E is the magnitude of the scattered electric field and E_0 is the magnitude of the incident electric field. In figures 1(a) and (b) the insets show the 2D cross-section of FE distribution, where the colour legend shows the magnitude of the FE factor. As shown in this figure, the optimal size to achieve maximum FE occurs at 130 nm in diameter, with an AR = 0.8 for CSNPs (~E/E_0 = 7.8), and at 150 nm in diameter for SNPs (~E/E_0 = 5.1). Figures 1(c) and (d) show calculated absorption, scattering and extinction spectrum for CSNPs with diameter = 130 nm and AR = 0.8, and for SNPs with diameter = 150 nm, where the absorption cross-section at $\lambda = 800$ nm is $\sigma_{abs} = 1.25 \times 10^4$ nm^2 and $\sigma_{abs} = 0.25 \times 10^4$ nm^2 for CSNPs and SNPs, respectively. The small and the main peaks in figure 1(c) near 590 nm and 730 nm and in figure 1(d) near 530 nm and 630 nm is due to the role of dipole and quadrupole plasmon resonance, respectively.

In figures 1(e) and (f) we study and compare the impact of particles' diameters on the absorption cross section at $\lambda = 800$ nm for CSNP with AR = 0.8 and SNP, respectively. As shown in these figures, the absorption cross section in the SNPs is around one order of magnitude smaller than that in the CSNPs. It is important to mention that this absorption cross section in figures 1(e) and (f) could behave in a different manner if we were looking at a different wavelength, depending on how close the wavelength is to the plasmon resonance peak.

To show the impact of AR for CSNP, in the inset of figure 1(a) we show the change in field enhancement with respect to the AR for a gold CSNP with a diameter of 130 nm. It is important to note that the strongest FE near the CSNP's surface happens when the AR is around 0.85. Also, the stronger the FE factor, the more plasma formation occurs
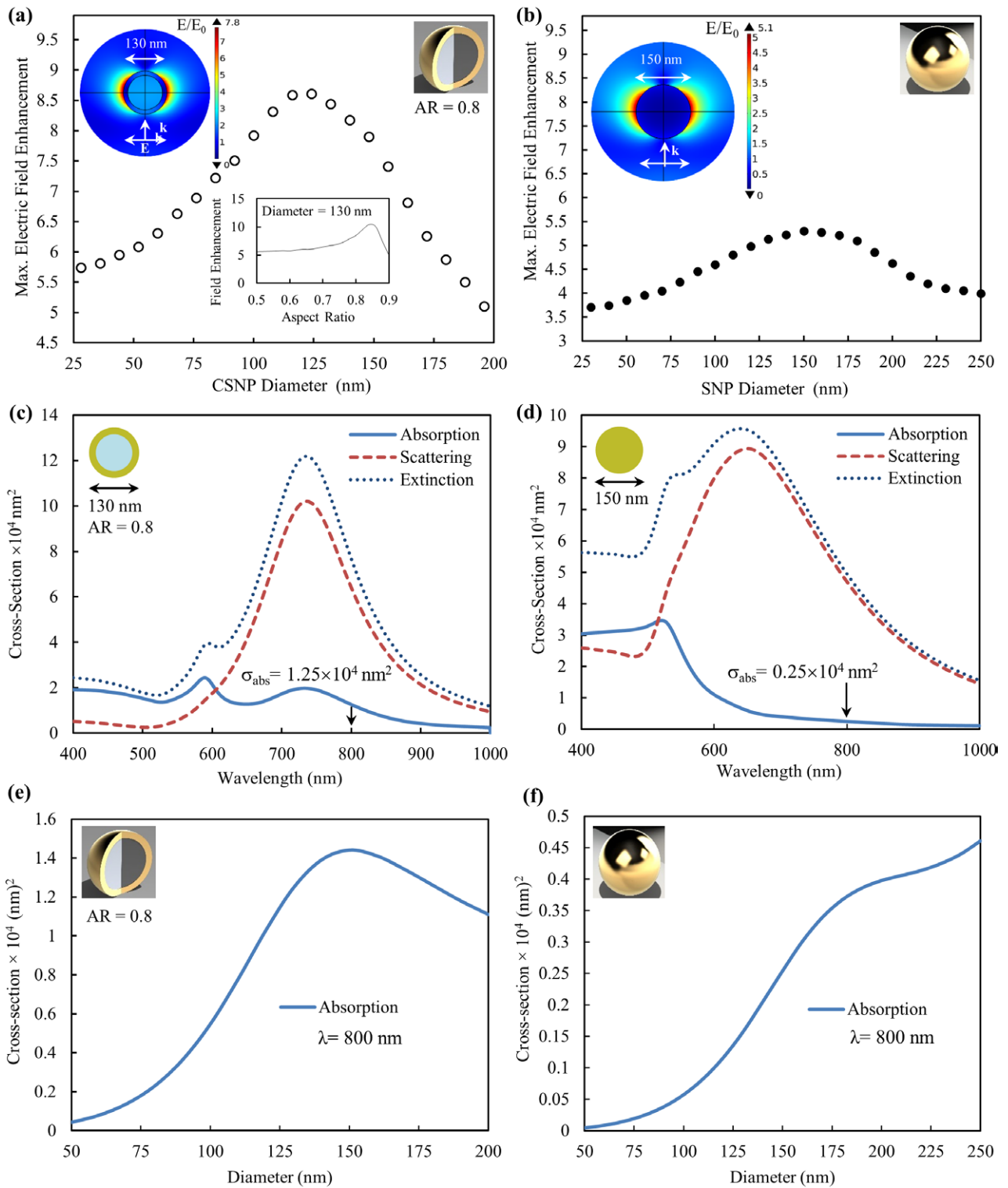
Figure 1. Calculated maximum near-FE factor (scattered field amplitude divided by incident field amplitude) of (a) CSNP and (b) SNP in water at off-resonance wavelength $\lambda = 800$ nm versus particle size. The insets show their corresponding electric FE distribution cross-sections for the particles with the highest FE values. The colour legend on the right shows the magnitude of the FE factor (E/E_0). (c) and (d) show FEM calculation of scattering, absorption and extinction cross-sections as a function of the incident laser wavelength for a CSNP with diameter of 130 nm and AR of 0.8 and for an SNP with diameter of 150 nm. (e) and (f) show absorption cross-sections as a function of particle diameter for CSNP and SNP, respectively.

around the particle. Increasing the AR value to 0.85 however, leads to shifting the absorption cross-section at wavelength $\lambda = 800$ nm to a much higher value, to or close to the absorption peak. For example, for a CSNP with a diameter of 130 nm

and AR = 0.85, the absorption cross-section peak occurs exactly at $\lambda = 800$ nm. Therefore, we chose AR = 0.8 to take advantage of the relatively strong FE factor while avoiding the peak of the absorption cross-section.

J. Phys. D: Appl. Phys. **49** (2016) 105401

A Hatef *et al*

Energy deposition in gold NPs and in the surrounding induced plasma

In this section we compare the linear energy deposition in CSNP and SNP with the energy deposition in their surrounding induced plasma. Figure 2 shows this comparison in a CSNP with a diameter of 100 nm and an AR = 0.8, and in an SNP with a diameter of 100 nm. In this figure the energy deposition in both the gold NPs and their induced plasma has been graphed versus the fluence of a 45 fs laser at $\lambda = 800$ nm. As mentioned in the theory section, the energy deposition in plasma is calculated by the numerical integration of the total power absorbed by the plasma over the time-interval for the pulsed laser. We calculate the total power by numerical volume integration of the ionization and ohmic power density in the surrounding medium. As seen in figure 2, the cross point of energy deposition in the gold NPs and plasma occurs at fluences of 47 mJ cm^{-2} and 70 mJ cm^{-2} with the values of 2 pJ and 0.35 pJ for CSNPs and SNPs, respectively. This means that at the same size, the cross point for CSNPs occurs at a lower fluence but has a greater energy deposition in the plasma compared to SNPs. This is due to the nonlinear dependency of the energy deposition in plasma to the near field intensity. Therefore, as shown in the insets of the figures 2(a) and (b), we expect to see a greater energy deposition in the plasma associated with CSNPs since the FE distribution cross-sections of the CSNPs is greater than that of the SNPs.

Figure 3 compares the energy deposition in CSNPs and SNPs, and in the surrounding induced plasma versus laser fluence for different sizes of particles (diameter). As one can see in the case of CSNPs, for the chosen fluence range from 30 to 50 mJ cm^{-2}, energy depositions in the CSNPs and in the surrounding plasma are in the same order of magnitude. However, the deposited energy in SNPs is much smaller than that in the surrounding plasma.

In figure 4, we show the optimization of the energy deposition in the surrounding plasma versus gold NPs' diameters for different fluences. In the case of CSNPs, the optimized energy deposition occurs in the CSNP with a diameter of 130 nm. This trend can be explained based on the fact that for any fluence, the maximum FE happens at that same CSNP size (see figure 1(a)). On SNPs however, the optimized energy deposition happens in the SNPs with diameter of 170 nm. It is important to note that the maximum FE in SNPs happens at the diameter of 150 nm. Therefore, one may expect to see the maximum energy deposition in plasma at that same size. This apparent contradiction happens because the enhanced scattered electric field is distributed in a greater volume around SNPs and more ionization is expected in that region.

To compare the dependency of the energy deposition within CSNPs and the surrounding plasma on the particle size, in figure 5, we plot both energy depositions for two fluences of 35 and 50 mJ cm^{-2}. As shown in this figure, for 35 mJ cm^{-2}, there is no intersection for the energy deposition in CSNP and in plasma; however, increasing the fluence to 50 mJ cm^{-2} leads to two cross points at ~75 nm and ~155 nm. In figure 5(b), we calculate the ratio of the energy deposition in plasma to the energy deposition in CSNP for different particle sizes and laser fluences. In this figure, the cross points are shown by a horizontal dotted line indicating that there are no intersections for smaller fluences, and that they appear with the increase in fluence. Please note that the maximum of this ratio occurs at the radius of 120 nm for all fluences. Hence, in order to have a considerable energy deposition in plasma greater or comparable to that in the CSNP, a particle with the diameter of 120 nm and a fluence more than 35 mJ cm^{-2} can be chosen. This means that choosing any gold CSNP with a diameter extensively lower or higher than 120 nm and with a (45 fs, wavelength = 800 nm) laser fluence less than 35 mJ cm^{-2} will not generate sufficient plasma that can be considered as a reliable source of energy.

Thermodynamic analysis

As mentioned in the theory section, the two-temperature model (TTM) is used to describe the thermal evolution of the system. TTM is often used to describe the interaction between metals and ultrashort laser pulses. Following the irradiation, a non-equilibrium state arises between the quasi-free electrons of the metal and its quasi-ions. It is thus, usually considered that the gold NP is actually composed of two subsystems, one of electrons, and one of phonons, interacting together [32]. The thermal equilibrium in the electron gas and the thermal equilibrium in the phonons system are reached in a time much shorter than the electron–phonon interaction time (a few hundred of fs versus a few ps), which allow us to define two distinct temperatures for the quasi-free electrons and for the gold atoms, coupled by two hyperbolic equations. As the gold atoms are distributed on a crystal lattice, the temperature of the atoms is often referred to as the lattice temperature. The review article [32] explains clearly how this TTM is extended to femtosecond pulses and nanoscale structures.

The water molecules collision time and the phonon–phonon interaction time in the gold NPs are of about a few picoseconds to ~100 ps depending on the laser fluence and the geometry of NPs [33, 34]. The energy deposition in the plasma happens in a sub-picosecond timescale (45 fs pulse). It can therefore be assumed that water density remains constant during the first hundreds of femtoseconds [1], namely during the laser pulse and the beginning of the energy transfer from the plasma to water. The other thermodynamic variables will also start changing some time after the pulse is finished.

The thermodynamic parameters would definitely change the way the laser field interacts with the NP, if the pulse was long enough for the thermodynamic variables to change. With femtosecond excitation, the evolution takes place on too fast a pace. There is a nearly complete decoupling between the energy deposition and the resulting thermodynamic response. The near-field is thus only modified by the change in the electric permittivity (caused by the change in electronic density) following the laser irradiation, and not by those of the thermodynamic variables of the surrounding medium.

For the SNP and the applied 45 fs pulse with fluence ranging from 20 to 200 mJ cm^{-2} at wavelength $\lambda = 800$ nm, the absorption cross-section is relatively small compared to

J. Phys. D: Appl. Phys. **49** (2016) 105401

A Hatef *et al*
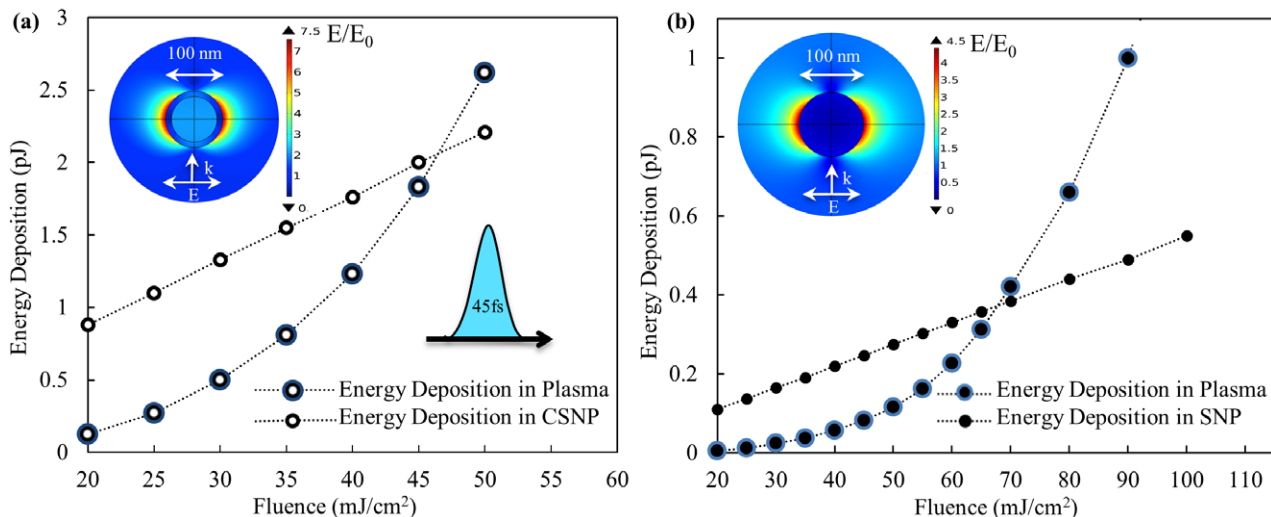
Figure 2. The cross point of energy deposition (pJ) in gold NPs and their surrounding induced plasma versus laser fluence with 45 fs pulse width at wavelength of 800 nm: (a) CSNP with diameter of 100 nm and AR = 0.8 and (b) SNP with diameter of 100 nm. The insets show their corresponding electric FE distribution cross-sections.
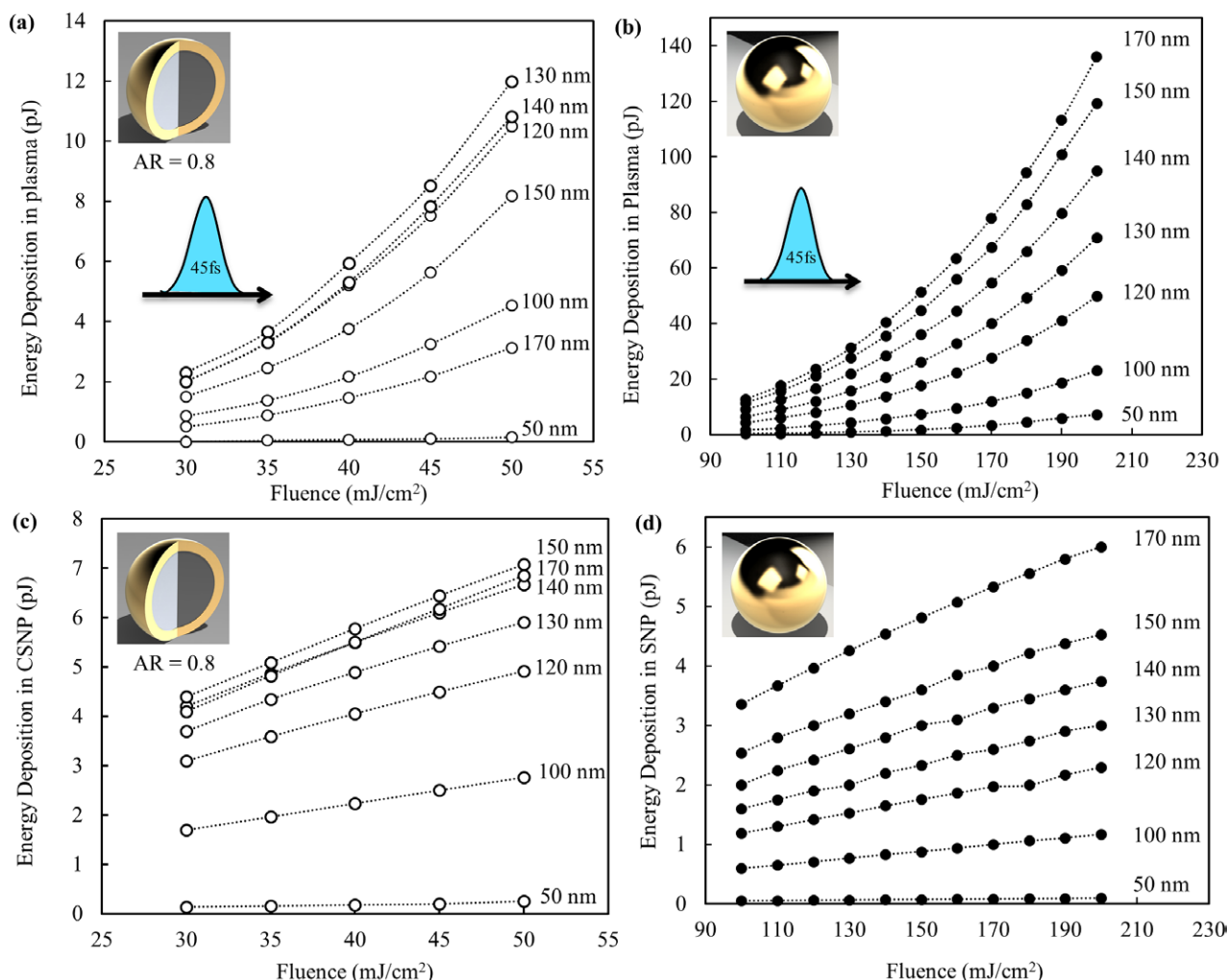
Figure 3. (a), (b) Energy deposition (pJ) versus fluence in induced plasma around CSNP and SNP respectively. (c), (d) Energy deposition versus fluence in CSNP and SNP respectively. The data is obtained for different particle sizes (diameter) by applying a 45 fs pulsed laser at wavelength of 800 nm.

J. Phys. D: Appl. Phys. **49** (2016) 105401

A Hatef *et al*
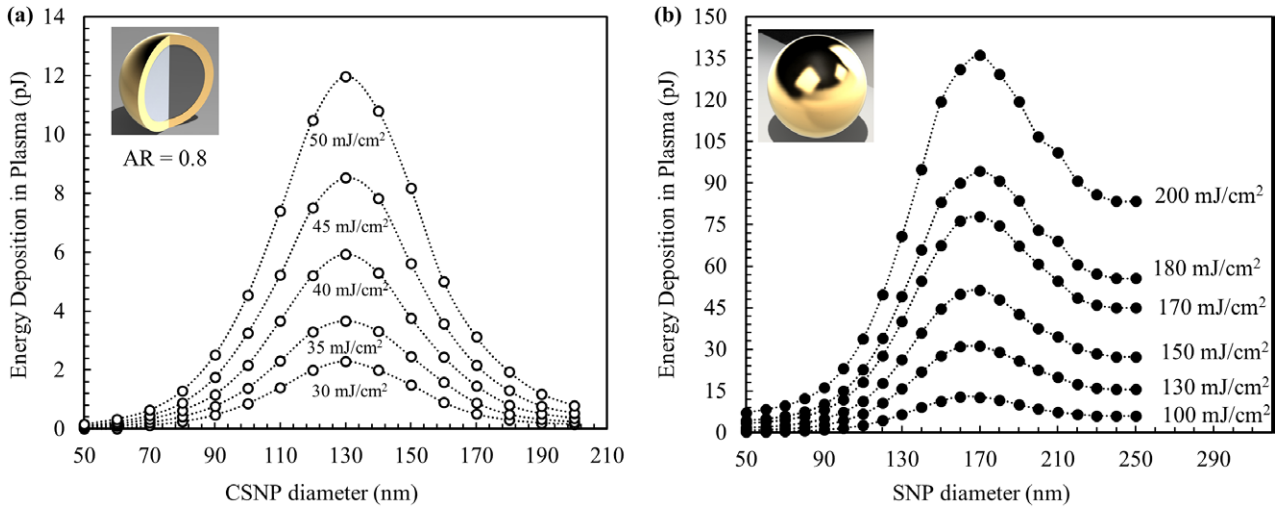
Figure 4. (a), (b) Energy deposition (pJ) in induced plasma around CSNPs and SNPs versus particle size for different fluences of a 45 fs laser at wavelength of 800 nm.
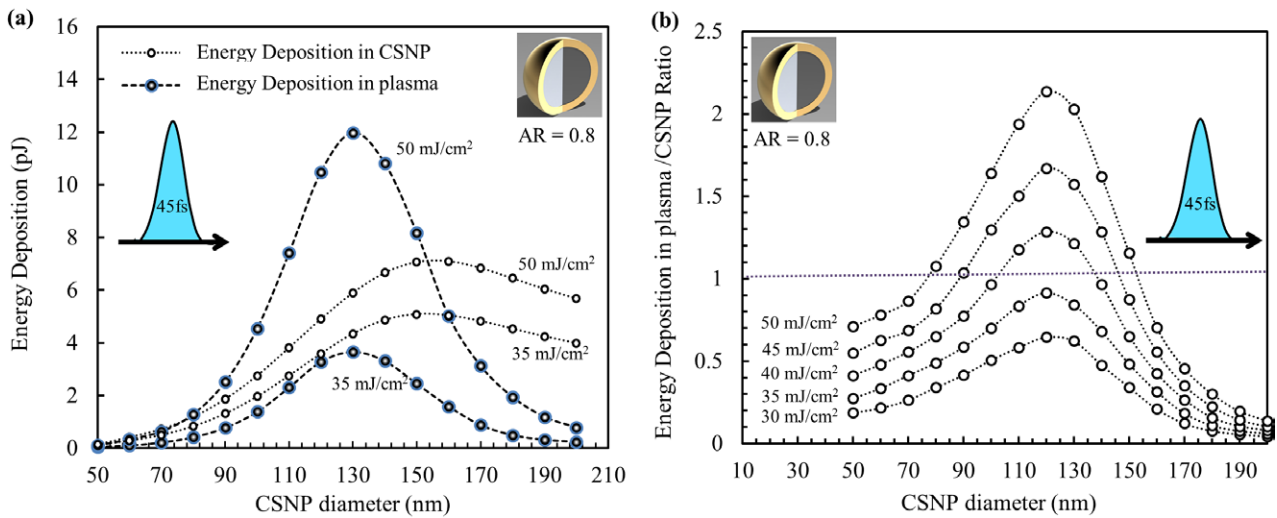
Figure 5. (a) Energy deposition (pJ) in CSNPs (AR = 0.8) of different sizes and in the surrounding induced plasma, for 45 fs pulsed laser fluences of 35 and 50 mJ cm^{-2} at wavelength of 800 nm. (b) The ratio of energy deposition in plasma to the energy deposition in CSNPs (AR = 0.8) of different sizes and fluences.

that in shorter wavelengths. As a result, the particle never reaches its melting temperature [3, 11, 16]. Therefore in our study, the thermal energy absorbed by the SNPs causes no fragmentation, deformation, or melting; preserving the integrity of the particles.

On the other hand, for CSNPs, our calculations show that for the considered range of fluences (20 to 50 mJ cm^{-2}), the particle temperature exceeds the critical melting point of the bulk gold [16]. Therefore, in such circumstances, we can only rely on a one-shot process where the particle melts or is destroyed after being irradiated once. The fluence range is taken from 20 to 50 mJ cm^{-2} in order to generate sufficient free electron density around the particle and make the energy deposition in the plasma comparable to or greater than the energy deposition in the CSNPs. Please note that our model is only capable of calculating the energy deposition in generated plasma and in the gold NP assuming that the NP stays intact during the pulse. Therefore, for CSNPs,

other photomechanical mechanisms such as melting (including the latent heat) and fragmentation can be added to the model.

In figure 6, we provide the temperature profile for the interface between the gold NPs and the surrounding medium. Both CSNP and SNP in this figure have been irradiated with a 45 fs pulsed laser at wavelength $\lambda = 800$ nm. However, the CSNP (with diameter = 130 nm and AR = 0.8) in figure 6(a) is irradiated with a laser fluence of 50 mJ cm^{-2} while the SNP (diameter = 170 nm) is irradiated with that of 200 mJ cm^{-2}. The lattice temperature increase in figures 6(a) and (b) reaches 2720 K and 865 K, respectively.

In the case of any interest in taking advantage of the energy deposition in the plasma around CSNPs, we recommend using hollow CSNPs to avoid any fragmentations. It has been shown that if the fluence of the incident laser is above the threshold and causes any melting, the hollow CSNPs collapse and form smaller SNPs [35].

J. Phys. D: Appl. Phys. **49** (2016) 105401

A Hatef *et al*
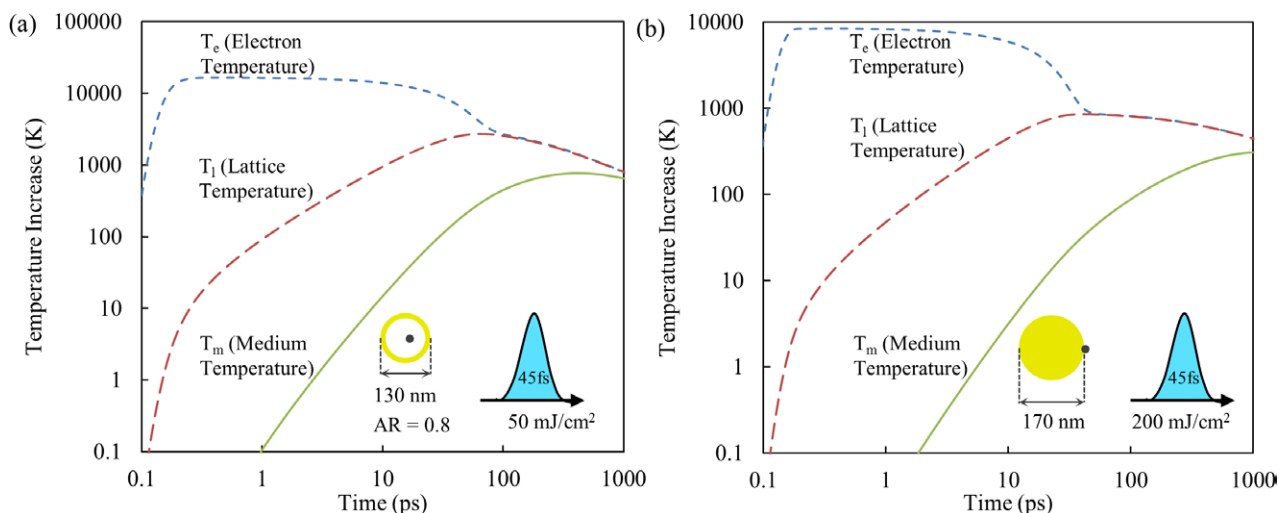
Figure 6. Time dependent temperature evolution of electrons (T_e), lattice (T_l) and water temperature (T_m), at the gold NP–water interface, for a laser pulse of 45 fs at wavelength $\lambda = 800$ nm with a fluence of (a) 50 mJ cm^{-2} and (b) 200 mJ cm^{-2} for a CSNP with a diameter of 130 nm and AR = 0.8 and for an SNP with diameter of 170 nm, respectively.

Conclusion

In summary, in this paper, we presented a numerical framework to simulate the energy deposition within spherical gold nanoparticles (core–shell and solid nanoparticles) and the induced surrounding plasma. The particles are immersed in water and are irradiated by an ultra-short (45 fs) pulsed laser in the tissue therapeutic optical window ($\lambda = 800$ nm). Enhanced by the nanoparticles, the intensity of the scattered near field can induce formation of electronic plasma. Here, we make a comparison between the impact of the geometrical parameters of both nanoparticles and the incident laser fluence on the energy deposition in plasma and nanoparticles. Our results show that for a core–shell nanoparticle, the cross point between the photothermal energy deposition in the nanoparticle and the induced plasma occurs at a higher energy and a lower fluence than that in the solid nanoparticle with same size and corresponding induced plasma. However, for the applied range of laser fluences that lead to plasma formation, the lattice temperature in core–shell nanoparticles exceeds the melting point and the particles integrity cannot be guaranteed after a single laser pulse. This is due to the higher absorption cross section of the core–shell nanoparticles compared with that of the solid nanoparticles at $\lambda = 800$ nm. In conclusion, for applications where integrity of the nanoparticles is not a priority, the energy deposition in plasma can be drastically boosted with core–shell nanoparticles with a diameter of 130 nm and AR of 0.8. On the other side, with solid nanoparticles, one can rely on remarkable energy deposition in the plasma well below the thermal destabilization threshold for the particles with a diameter of 170 nm. We also emphasize that our model is to show the energy deposition in the gold nanoparticles and surrounding plasma during an ultrashort pulse laser irradiation. In this model we assumed that the nanoparticles stay intact during the pulse; however, the photomechanical mechanisms underlying pressure waves, melting (including latent heat) and possible fragmentation can be added to the model. In this

way the thermal and mechanical dynamics following laser irradiation can be controlled to optimize the desired biomedical application.

References

[1] Vogel A, Noack J, Hüttman G and Paltauf G 2005 *Appl. Phys. B* **81** 1015
[2] Hoy C L, Ferhanoglu O, Yildirim M, Kim K H, Karajanagi S S, Chan K M C, Kobler J B, Zeitels S M and Ben-Yakar A 2014 *IEEE J. Sel. Top. Quantum Electron.* **20** 242
[3] Boulais É, Lachaine R and Meunier M 2012 *Nano Lett.* **12** 4763
[4] Saha K, Agasti S S, Kim C, Li X, Rotello V M 2012 *Chem. Rev.* **112** 2739
[5] Jing-Liang L and Min G 2010 *IEEE J. Sel. Top. Quantum Electron.* **16** 989
[6] Huang X and El-Sayed M A 2010 *J. Adv. Res.* **1** 13
[7] Schomaker M, Heinemann D, Kalies S, Willenbrock S, Wagner S, Nolte I, Ripken T, Escobar H, Meyer H and Heisterkamp A 2015 *J. Nanobiotechnol.* **13** 10
[8] Hatef A and Meunier M 2015 *Opt. Express* **23** 1967
[9] Erickson T A and Tunnell J W 2007 *Nanotechnologies for the Life Sciences* (New York: Wiley)
[10] Hainfeld J F, O'Connor M J, Lin P, Qian L, Slatkin D N and Smilowitz H M 2014 *PLoS One* **9** e88414
[11] Lachaine R, Boulais É and Meunier M 2014 *ACS Photon.* **1** 331
[12] Boutopoulos C, Bergeron E and Meunier M 2016 *J. Biophoton.* **9** 26
[13] Jackson J 1998 *Classical Electrodynamics* 3rd edn (New York: Wiley)

J. Phys. D: Appl. Phys. **49** (2016) 105401

A Hatef *et al*

[14] Peter Y Yu and Cardona M 2010 *Fundamentals of Semiconductors, Physics and Materials Properties* (New York: Springer)

[15] Mitra J, Lei F, Michael G B and Dawson P 2009 *J. Phys. D: Appl. Phys.* **42** 215101

[16] Boutopoulos C, Hatef A, Fortin-Deschenes M and Meunier M 2015 *Nanoscale* **7** 11758

[17] Changhong L, Mi C C and Li B Q 2008 *IEEE Trans. NanoBiosci.* **7** 206

[18] Hashimoto S, Werner D and Uwada T 2012 *J. Photochem. Photobiol.* C **13** 28

[19] Johnson P B and Christy R W 1972 *Phys. Rev.* B **6** 4370

[20] Date H, Sutherland K L, Hasegawa H and Shimozuma M 2007 *Nucl. Instrum. Methods Phys. Res.* B **265** 515

[21] Arnold C L, Heisterkamp A, Ertmer W and Lubatschowski H 2008 *Proc. SPIE* **6881** 688104

[22] Ashcroft N M and Mermin N D 1976 *Solid State Physics* (Fort Worth, TX: Harcourt College Publishers)

[23] Bellan P 2006 *Fundamentals of Plasma Physics* (Cambridge: Cambridge University Press)

[24] Lee Y T and More R M 1984 *Phys. Fluids* **27** 1273

[25] Hallo L, Bourgeade A, Tikhonchuk V, Mezel C and Breil J 2007 *Phys. Rev.* B **76** 024101

[26] Veysman M, Cros B, Andreev N E and Maynard G 2006 *Phys. Plasmas* **13** 053114

[27] Maksimova I L, Akchurin G G, Khlebtsov B N, Terentyuk G S, Akchurin G G, Ermolaev I A, Skaptsov A A, Soboleva E P, Khlebtsov N G and Tuchin V V 2007 *Med. Laser Appl.* **22** 199

[28] Oldenburg S J, Averitt R D, Westcott S L and Halas N J 1998 *Chem. Phys. Lett.* **288** 243

[29] Scholl J A, Koh A L and Dionne J A 2012 *Nature* **483** 421

[30] Alvarez M M, Khoury J T, Schaaff T G, Shafigullin M N, Vezmar I and Whetten R L 1997 *J. Phys. Chem.* B **101** 3706

[31] Vogel A and Venugopalan V 2003 *Chem. Rev.* **103** 577

[32] Singh N 2010 *Int. J. Mod. Phys.* B **24** 1141

[33] Link S and El-Sayed M A 2000 *Int. Rev. Phys. Chem.* **19** 409

[34] Sun C K, Vallée F, Acioli L H, Ippen E P and Fujimoto J G 1994 *Phys. Rev.* B **50** 15337

[35] Wu G, Mikhailovsky A, Khant H A and Zasadzinski J A 2009 *Methods in Enzymology* ed D Nejat (New York: Academic) p 279